Supporting Information: Towards broadband mechanical spectroscopy

Tina Hecksher,[1, a)] Darius H Torchinsky,[2, a)] Christoph Klieber,[3, a)] Jeremy A. Johnson,[3, a)] Jeppe C. Dyre,[4] and Keith A. Nelson[3]

[1)] *Glass and Time, IMFUFA, Dept. of Science and Environment, Roskilde University, DK-4000 Roskilde, Denmark*

[2)] *Department of Physics, MIT, Cambridge, MA 02139, USA*

[3)] *Department of Chemistry, MIT, Cambridge, MA 02139, USA*

[4)] *DNRF Centre Glass and Time, IMFUFA, Dept. of Sciences, Roskilde University, DK-4000 Roskilde, Denmark*

I. EXPERIMENTAL METHODS

Overview over the seven different measurement methods and the frequency ranges that they cover are summarized in Fig. S1; detailed descriptions of the techniques and data collected from them are discussed in the subsequent sections below. The techniques include three low-frequency methods involving piezo-ceramics that shear or compress the entire sample quasi-statically[S1–S4] and four higher-frequency methods utilizing short laser pulses to excite and subsequently detect acoustic waves in an irradiated region[S5–S11].
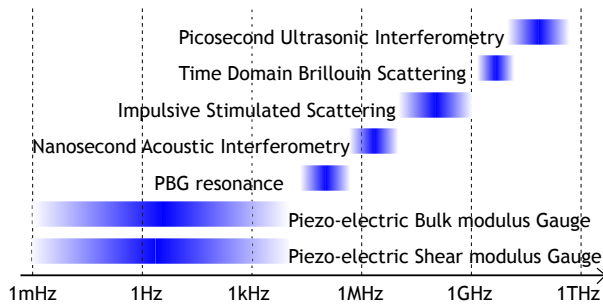

FIG. S1. Survey of mechanical spectroscopic techniques. At low frequencies (from mHz up to ~ 10 kHz) the piezo-electric Shear modulus Gauge (PSG) and the piezo-electric bulk modulus Gauge (PBG) were used to measure the shear and bulk moduli. Analysis of the overtones in the PBG provided access to some data points in the $100 - 500$ kHz region. In the low MHz range, nanosecond acoustic interferometry (NAI) was used to probe the frequency dependence of the longitudinal sound speed and attenuation rates directly. In the higher MHz range, impulsive stimulated scattering (ISS) was used to measure longitudinal sound velocities and damping at specified acoustic wavevectors. Finally, time-domain Brillouin light scattering (TDBS) and picosecond ultrasonic interferometry (PUI) were used to measure longitudinal acoustic speeds and attenuation in the MHz-GHz frequency ranges shown.

[a)]These authors contributed equally.

A. Low-frequency methods

The low-frequency methods measure mechanical moduli directly. These techniques do not measure the longitudinal modulus, but the bulk and shear moduli. In the isotropic case (e.g., in a liquid) there are only two unique mechanical moduli, and the longitudinal modulus M is given in terms of the bulk (K) and shear (G) moduli as: $M = K + 4/3G$.
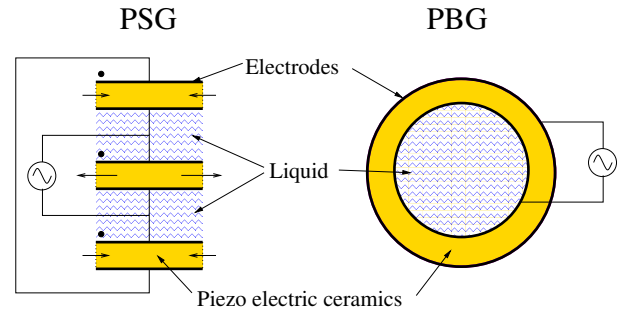

FIG. S2. Schematic drawing of the PSG and PBG. In the PSG three electrode-covered piezo-electric ceramic discs are mounted in a layer construction; the liquid is loaded into the gaps between the discs. In the PBG, a spherical shell of piezo-electric ceramic material is filled with the liquid via a hole drilled in the ceramics. A liquid reservoir (not shown here) is attached above the hole, allowing extra liquid to be drawn in as the temperature is lowered.

Both the piezo-electric shear modulus gauge (PSG) and the piezo-electric bulk modulus gauge (PBG) methods are based on the piezo-electric effect, i.e., the conversion of electrical to mechanical energy. These methods have been documented in detail by Christensen and Olsen in Refs. S3 and S2, respectively. In the following we briefly sketch the steps in modeling of the devices, which allow us to deduce a mechanical modulus from the electrical data.

1. Piezo-electric Shear Modulus Gauge

The PSG is constructed of three electrode-covered piezo-electric ceramic discs mounted in a layered construction, which prevents unwanted bending of the discs and further has the advantage that it can be mapped

mathematically to a one-disc system involving a fixed wall[S3].

The liquid is loaded into the 0.5 mm gap between the discs (Fig. S2). Depending on the polarity of the discs as compared with the direction of an applied electric field, the discs expand or contract in the radial direction. Electrically, the middle disc is connected in parallel with the two outer discs in series as shown in Fig. S2. Here, the small dots indicate the polarity of the piezo-electric discs; thus when an electric field is applied, the middle disc moves in opposition to the two outer discs. With this construction the gap between the discs is field free, and the liquid is subjected to a purely mechanical perturbation.

The capacitance of each disc depends on its strain state, so if the liquid is partially clamping the disc (thus hindering its motion), the measured capacitance is lower than that of freely moving discs. By a precise measurement of the electrical capacitance of the PSG one can obtain the stiffness of the liquid in contact with the disc. In other words, knowing the exact relationship between the two, we can convert the electric impedance into the shear modulus.

The elasto-electric compliance matrix describes the connection between the components of the stress σ_{ij} and strain ϵ_{ij} tensors and the electrical field of the piezo-electric material. The equations describing a axially polarized ceramic can be split into four independent parts, the relevant components of which can be reduced to the following

$$\begin{pmatrix} \sigma_{rr} \\ \sigma_{\phi\phi} \\ D_z \end{pmatrix} = \begin{pmatrix} c_{11} & c_{12} & -e_{13} \\ c_{12} & c_{11} & -e_{13} \\ e_{13} & e_{13} & \varepsilon_{33}^S \end{pmatrix} \begin{pmatrix} \epsilon_{rr} \\ \epsilon_{\phi\phi} \\ E_z \end{pmatrix} \quad \text{(S1)}$$

where c_{11} and c_{12} are elastic constants of the ceramic, ϵ_{33}^S is the dielectric constant, and e_{13} is the coupling constant.

The measured capacitance C_m of the disc can be found by integrating the charge density D_z and dividing by the voltage

$$C_m = \frac{Q}{U} = \frac{\int_0^{r_0} 2\pi r D_z(r)\,dr}{\xi E_z}, \quad \text{(S2)}$$

where the charge density D_z is given by Eq. (S1) and ξ is the thickness of the disc. D_z depends both on the strain state and the applied electrical field E_z. Evaluating this integral it is found that the capacitance is a function of the radial displacement at the edge of the disc $u_r(r_0)$

$$C_m = A u_r(r_0) + B \quad \text{(S3)}$$

where A and B are known constants. It remains to determine the displacement at the edge of the disc $u_r(r_0)$ as a function of rigidity of the liquid. The displacement u_r is found by solving the radial equation of motion, which reduces to

$$c_{11}\left(r^2(u_r'') + u_r' - u_r\right) - \sigma_l \frac{r^2}{\xi} = -\omega^2 r^2 \rho u_r \quad \text{(S4)}$$
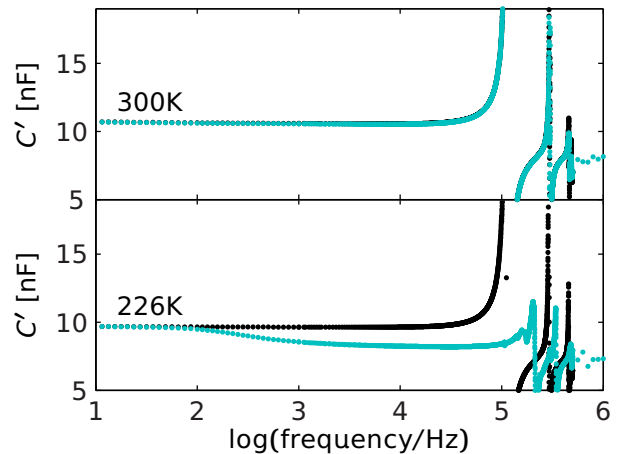

FIG. S3. Raw data of the empty (black) and liquid-filled (blue) PSG at two different temperatures. At 300 K the presence of the liquid does not affect the signal because the liquid is quite fluid. At 226 K the liquid partially clamps the discs, which is manifested as a drop in capacitance in the quasi-static region and a shift of the resonances in the high-frequency region.

where the prime indicates the derivative with respect to r, ξ is the thickness of the disc and σ_l is the tangential stress that the liquid exerts on the disc. σ_l is by definition proportional the shear modulus of the liquid $\sigma_l = G(\omega)u_r/d$, where d is the thickness of the liquid layer (or equivalently the distance between the discs), which is the quantity relevant to determining the relaxation.

Figure S3 shows the measured capacitance of the empty (black trace) and liquid-filled (blue trace) PSG. At high temperatures there is no influence from the liquid at these frequencies and the two spectra are identical. The resonances in the spectrum are mechanical resonances of the discs. At lower temperatures, the shear modulus of the liquid increases and partially clamps the discs. This is observed as a drop in the capacitance below the first resonances. We will refer to the range of frequencies below the first resonance (< 100 kHz) of the system as the *quasi-static* region. The liquid also influences the positions of the overtones as compared with the spectrum of the empty device. In the quasi-static region, the shear modulus is found via the described inversion procedure. The inverted data, i.e., the inferred complex shear modulus, are shown in Fig. S4.

2. Piezo-electric Bulk Modulus Gauge

The PBG, which was also depicted in Fig. S2, consists of a spherical shell of a piezo-electric ceramic material polarized in the radial direction. The shell is covered by an electrode material both on the inside and the outside. Applying an electric field to the capacitor, which these electrodes constitute, deforms the ceramic (expanding or
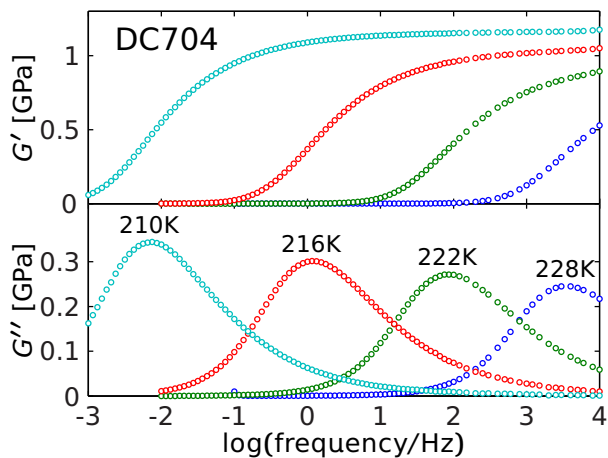
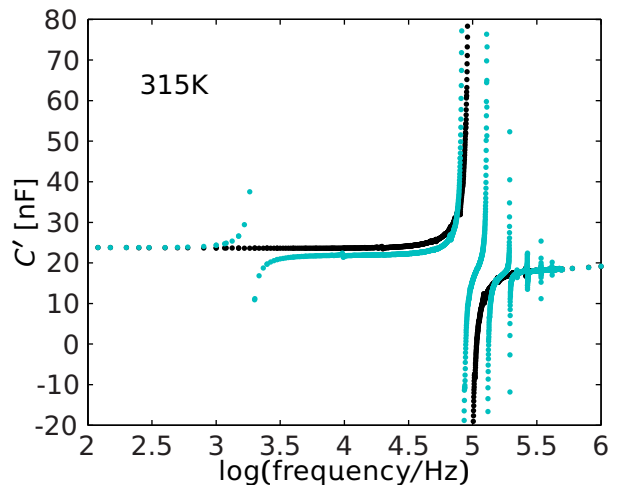FIG. S4. Real and imaginary parts of the shear modulus of DC704 at four temperatures approaching T_g.

FIG. S5. Raw data of the empty (black) and the liquid-filled (blue) PBG. In the spectrum of the empty cell there is only one resonance (at ~ 100 kHz). There are a number of extra features that all come from the liquid. At low frequencies the capacitance of the two is the same. Around 1 kHz there is a small resonance, which comes from the liquid flowing in and out of the shell via a tube. Above that resonance the shell is partially clamped and the measured capacitance is reduced compared to that of the empty PBG. At frequencies above the first big resonance, the extra resonances are all due to standing waves in the liquid.

contracting depending on the direction of the field) and effectively changes the inner volume of the sphere.

A liquid inside the shell will oppose this deformation and thus change the measured capacitance. The difference in capacitance between the empty, freely moving shell and the partially clamped shell can be related to the bulk modulus of the liquid. The deformation is radial. An analysis of forced vibrations in a visco-elastic sphere shows that in the low-frequency (quasi-static) region of the measurement this corresponds to an isotropic compression of the liquid, while at high frequencies it is a mixture of bulk and shear deformations.

In order to be able to fill the PBG with liquid, a hole is drilled in the shell. A tube is attached over the hole. Filling this tube, as well as the entire shell, allows the PBG to draw in extra liquid when the liquid in the shell contracts during cooling. Thus the liquid volume is constant throughout the duration of the measurement, i.e., at all temperatures.

The modeling of the PBG is somewhat simpler than that of the PSG since one can assume that the thickness of the ceramic is negligible in the direction of its motion. Thus we can express the model in terms of an electrical equivalent diagram, shown in Fig. S6, where the conversion from electrical to mechanical energy is modeled by a transducer T_r. On the electrical side of the diagram there is a capacitor C_1 which corresponds to the actual capacitor constituted by the two electrodes. On the mechanical side, the capacitor C_2 models the elastic properties of the ceramic, the inductor L models the inertance, and the resistor R models the friction. The "black box" C_{liq} is the liquid capacitance which is what we want to determine.

The capacitance of the model depicted in Fig. S6 is given by

$$C_m(\omega) = C_1 + T_r^2 \frac{1}{\frac{1}{C_2} + i\omega R - \omega^2 L + \frac{1}{C_{\text{liq}}}}. \quad \text{(S5)}$$

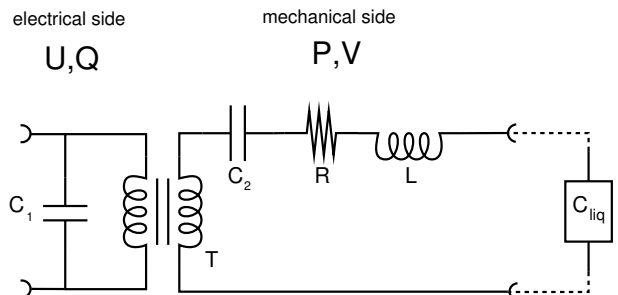All the constants C_1, C_2, L, R, T_r can be determined from

FIG. S6. Electrical equivalent model of the PBG. The transformer represents the conversion from electrical to mechanical energy in the piezo-electric ceramic. On the electric side of the network the capacitor is an actual capacitor that the electrodes constitute. On the mechanical side, an LCR series models the inertial, elastic, and dissipative properties of the ceramic. When the PBG is empty the mechanical port is short circuited, allowing the shell to move freely. The liquid-filled PBG is modelled with an extra box C_{liq} in series.

a measurement of the empty PBG. A subsequent measurement of the liquid-filled PBG allows for the determination of the liquid's mechanical stiffness $S_{\text{liq}} = 1/C_{\text{liq}}$ by isolating that term.

Next, we wish to express the stiffness in terms of the elastic moduli. The mechanical stiffness is $S_{liq} = \delta p / \delta V \approx -\sigma_{rr}(r_0)/4\pi r_0^2 u_r$. Solving the equation of motion for forced vibrations in a visco-elastic sphere one finds the displacement field u_r, which leads to the follow-
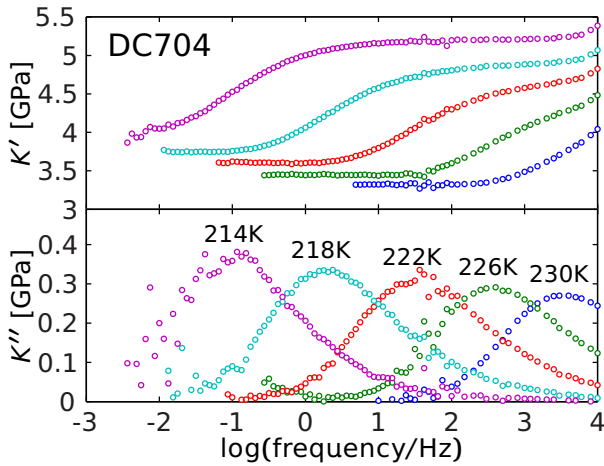
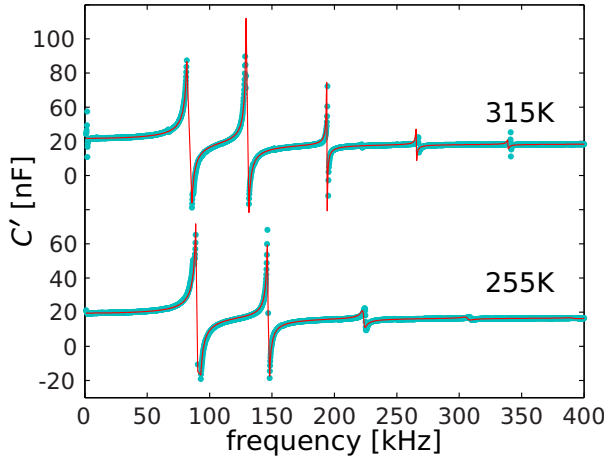FIG. S7. Real and imaginary parts of the bulk modulus of DC704 for selected temperatures close to T_g.

FIG. S8. Real part of capacitance in the resonance region of the PBG measurement. Data are blue dots and dashed lines are fits of a Eq. (S6) in combination with the model in Eq. (S5).

ing expression for the stiffness of the liquid[S2]

$$S_{\text{liq}} = \frac{1}{V}\left[K - M\left(1 + \frac{1}{3}\frac{x^2 \sin x}{x \cos x - \sin x}\right)\right]. \quad \text{(S6)}$$

Here V is the volume of the sphere, K and M are the (adiabatic) bulk and longitudinal moduli, and $x = \sqrt{\rho/M}r_0\omega$. We have $S_{\text{liq}} \to K/V$ as $\omega \to 0$, i.e., in the quasistatic region we are measuring the bulk modulus. The inverted complex bulk modulus data for DC704 are shown in Fig. S7.

At high frequencies we can fit Eq. (S6) in conjunction with Eq. (S5) to the resonances, at least at high temperatures where we can assume $K = K(\omega \to 0) = M(\omega \to 0)$ and the viscosity to be frequency-independent. Fits to data in the resonance region are shown in Fig. S8.
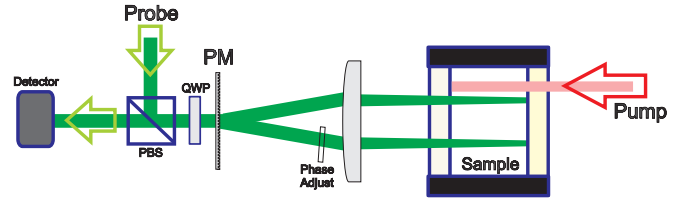

FIG. S9. Nanosecond acoustic interferometry setup. A pump pulse is absorbed weakly in the sample, and sudden heating and thermal expansion generate a cylindrical acoustic wave radiating outwards from the pump beam. This acoustic pulse passes successively through each arm of a grating interferometer, and time-dependent changes in refractive index translate to time-dependent intensity of the interferometrically recombined signal.

B. Nanosecond Acoustic Interferometry

In Nanosecond Acoustic Interferometry (NAI) acoustic wavepackets with a distribution of frequency components in the low MHz range are generated by a picosecond duration pump beam loosely focused in the sample. Weak absorption leads to heating and thermal expansion of the excited region, impulsively generating an outward propagating cylindrical wave[S12,S13]. This wave is sequentially detected at the two arms of grating interferometer[S14,S15] due to the phase difference created by density-mediated changes in the refractive index. The interferometer arms are recombined at a diffraction grating, and we measure time-dependent changes in the intensity of the resulting single beam directed to a detector.

The setup is depicted in Fig. S9. To achieve maximum sensitivity, the incoming continuous wave probe beam passes through a polarizing beam splitting cube (PBS) and then a quarter waveplate (QWP) to induce circular polarization. After passing through the diffractive optic (binary phase mask pattern: PM), the ± 1 diffraction orders are brought parallel and focused by a lens through the sample cell to a dichroic mirror at the back of the sample, which reflects the probe beams and transmits the pump. The returning beams recombine at the phase mask, pass again through the QWP, and the resulting single beam is of correct polarization for transmission through the PBS to a fast detector. A glass plate in the path of one interferometer arm was rotated for relative phase control. Signals were recorded at the relative phases $-\pi/2$ and $\pi/2$, midway between maximum constructive and destructive interference, where the induced phase change, and therefore the detected response, was greatest[S15].

Figure S10(a) shows a recorded trace of an acoustic pulse generated in liquid DC704 passing through the first probe arm at $t = 0$ and the second at later times. The inset shows the Fourier amplitude of the pulse at each point, where the attenuation of the wave is apparent through the relative change in spectral amplitude. In Fig. S10(b), we show traces recorded at a number of dif-

The velocity and attenuation of the excited frequency components are determined using the Fourier transform of the acoustic pulse at each detection point according to

$$\tilde{f}(\omega) = \mathcal{F}(f(t)) = \frac{1}{\sqrt{2\pi}} \int_{-\infty}^{\infty} f(t)e^{-i\omega t}dt\,. \qquad (S7)$$

Using the shift theorem, i.e., that $\mathcal{F}(f(t - a)) = e^{-i\omega a}\tilde{f}(\omega)$, and the distance d between interferometer probe arms, we can recover the speed of sound for the excited frequency components via the phase. The acquired phase (ϕ) of the Fourier transform is ωa, and thus by taking the derivative of the phase ($\partial_\omega \phi$) with respect to frequency, we recover the frequency-dependent shift in time $a(\phi)$. Using the Fourier transforms of the wavepacket at the first probe point and second probe point, we can determine the frequency-dependent sound speed via

$$v(\omega) = \frac{d}{\delta t(\omega)} = \frac{d}{\partial_\omega\phi_1(\omega) - \partial_\omega\phi_2(\omega)}. \qquad (S8)$$

where the subscripts 1 and 2 refer to the first and second probe point, respectively. In practice, the amplitude of the phase recovered from a numerical Fourier transform may depend on the number of time points in the time-domain trace, and so we needed to multiply Eq. S8 by a constant calibration factor. All recorded traces contained an identical number of time points, and therefore a single calibration factor for all analysis was sufficient. The calibration factor was picked to recover the sound speed of the solid phase determined at low temperatures from the PBG/PSG and ISS data; this calibration factor also recovered the liquid sound speed at high temperatures (in comparison to ISS data), and so we use it with confidence for all temperatures. All points presented here were also collected with the same probe distance d, which can be determined using the grating period and the lens focal distance according to

$$d = 2f \tan\left(\sin^{-1}\left(\frac{\lambda_p}{2\Lambda}\right)\right)\,, \qquad (S9)$$

where f is the lens focal length, λ_p is the probe wavelength, and Λ is the grating period. Using our experimental parameters of a 532 nm probe wavelength, 85 mm lens focal length, and 8.5 μm grating period, this translated to $\sim$ 5 mm distance between probe beams which agreed with a physical measurement of the distance.

The frequency-dependent acoustic attenuation $\gamma(\omega)$ can be determined by the amplitude of the Fourier transform of the acoustic pulse at each probe point according to the Beer-Lambert law as

$$\alpha(\omega) = \frac{\ln(|\tilde{f}_2(\omega)|/|\tilde{f}_1(\omega)|)}{d}. \qquad (S10)$$

Here $|\tilde{f}_i(\omega)|$ denotes the magnitude and ϕ_i denotes the phase of the complex Fourier transform of the acoustic pulse at each point. As we used a round excitation spot to generate cylindrical acoustic waves with a well-defined
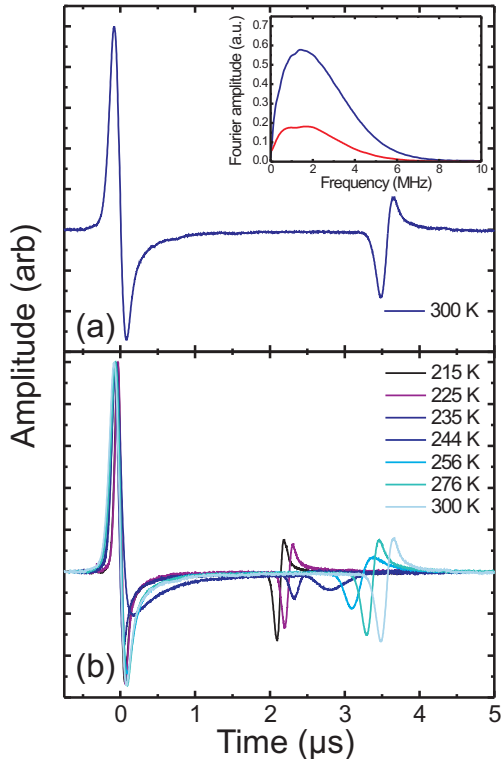

FIG. S10. (a) NAI trace recorded in DC704 at room temperature. A pump pulse is absorbed in the sample, generating a cylindrical wave radiating outwards. We observe the acoustic pulse passing first through one probe point and then through the second, where the amplitude reduction is clearly observed. The inset shows the Fourier amplitude of the pulse at the first (blue curve) and second (red curve) points. (b) Nanosecond acoustic interferometry measurements for different temperatures.

ferent sample temperatures for a set of traces normalized to the maximum amplitude.

The effect of the coupling of structural relaxation to the acoustic waves is twofold. First, we observe that as temperature is decreased, the wavepacket arrives at the second probe point more quickly, corresponding to an increasing speed of sound at lower temperatures. Second, we note that the amplitude of the wavepacket has a strong temperature dependence; acoustic damping is relatively low at high temperatures in the liquid state, but as temperature is reduced, strong damping is evident due to the alpha-relaxation. As temperature is decreased further, the alpha-relaxation shifts to lower frequencies and the damping is reduced at the acoustic frequencies of our measurement where we see a solid-like response. We note that even in the absence of acoustic damping, the amplitude of the pulse at the second probe point decreases solely due to the divergent nature of the cylindrical wavepacket, which is accounted for in the analysis below.

$r^{-1/2}$ reduction in amplitude, we account for the correction due to the acoustic wave divergence by the constant A, which is given in terms of d and the distance between pump spot and probe d_p as

$$A = \sqrt{\frac{d_p + d}{d_p}}. \qquad (S11)$$

We note that the attenuation is given here in units of inverse distance, whereas the damping rate is in units of inverse time; conversion between the two can be performed using the speed of sound.

For the broadband spectral analysis we can then construct the complex acoustic modulus by

$$M'(\omega) = \rho v^2(\omega) \frac{1 - (\alpha(\omega)v(\omega)/\omega)^2}{\left[1 + (\alpha(\omega)v(\omega)/\omega)^2\right]^2} \qquad (S12)$$

$$M''(\omega) = 2\rho v^2(\omega) \frac{\alpha(\omega)v(\omega)/\omega}{\left[1 + (\alpha(\omega)v(\omega)/\omega)^2\right]^2}, \qquad (S13)$$

which were the quantities used in our analysis below.

Determination of very weak attenuation coefficients becomes unreliable for a particular frequency when the signal-to-noise ratio in the Fourier domain is too low. In practice this was observed when, for a particular frequency in the Fourier domain, the ratio of the magnitude of the difference in acoustic signal amplitudes between the first and second detection points (the amplitude at the second point being corrected by the factor A) and the magnitude of the noise at the second detection point was lower than approximately three to one. For such low attenuation rates, the imaginary part of the modulus could not be determined.

C. Impulsive stimulated scattering

In an impulsive stimulated scattering (ISS) experiment conducted in a heterodyned four-wave mixing geometry, light from a pulsed laser is incident on a diffractive optical element, typically a binary phase mask (PM) pattern, and split into two parts (± 1 diffraction orders; other orders are blocked), which are recombined at an angle θ as depicted in Fig. S11. The crossed excitation pulses excite an acoustic wave with wavelength Λ given by the interference or "transient grating" period

$$\Lambda = \frac{\lambda_e}{2 \sin \theta/2} \qquad (S14)$$

where λ_e is the excitation laser wavelength. Probe light (in the present case from a CW diode laser) is also incident on a phase mask pattern (the same one or another with the same spatial period) and split into two parts, which are recombined at the sample to serve as probe
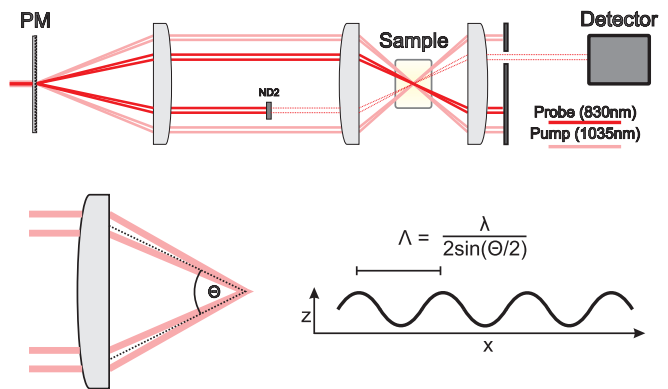

FIG. S11. Schematic illustration of the ISS setup. Both the pump and probe beams are incident on the phase mask (PM) and their ± 1 diffraction orders are recombined at the sample at an angle θ.

and reference beams. The signal arises from diffraction of probe light off the acoustic wave and any other spatially periodic responses induced by the excitation pulses. The diffracted signal field is superposed with the reference field for heterodyned time-resolved detection of the signal, which typically shows damped acoustic oscillations from which the acoustic frequency ω and damping rate Γ can be determined.

In an experiment where all four beams share common polarization V (denoted VVVV), the action of the excitation pulses is twofold. First, depending upon the absorbance at the pump wavelength, a fraction of the light is absorbed into the sample and this energy is very rapidly converted into heat. Sudden thermal expansion launches counter-propagating acoustic waves with the acoustic period Λ. In addition to acoustic oscillations, the signal may also show slower, nonoscillatory density responses and thermal diffusion from which complex structural relaxation dynamics and thermal diffusivities may be determined[S16]. This excitation mechanism is labeled Impulsive Stimulated Thermal Scattering (ISTS) and is the dominant mechanism in the VVVV measurements.

The second excitation channel arises from the electrostrictive work done on the liquid by the V-polarized excitations pulses. The electric field of the interference maxima both induces a polarization and does compressive work on the induced dipoles, resulting in impulsive excitation of counterpropagating longitudinal acoustic waves of wavelength Λ even in the absence of optical absorption. This excitation mechanism is termed impulsive stimulated Brillouin scattering (ISBS). As the force scales with the gradient of the light intensity, the efficiency of ISBS excitation scales as the acoustic wavevector $q = 2\pi/\Lambda$. Therefore this mechanism becomes more important as the scattering wavevector is increased.

The excitation pulses may also induce molecular orientational responses that can contribute to signal, analogous to depolarized quasielastic scattering[S7,S17], as well
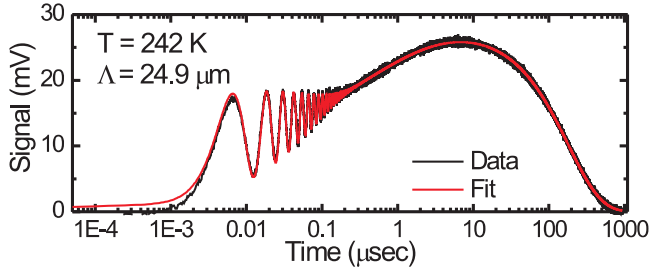
FIG. S12. ISTS signal in DC704 at 242K, 24.9 μm grating spacing. At short times, there is a damped acoustic oscillation due to counterpropigating acoustic waves. At later times, there is a slow rise due to the alpha-relaxation dynamics revealed though time-dependent thermal expansion. The signal eventually decays due to thermal diffusion of the thermal excitation grating.

as contributions due to flow. In order to avoid this complication, careful selection of the probe polarization relative to the grating wavevector direction was used to eliminate these contributions to signal.

The signal traces are fit to the model function[S16]

$$A\left(e^{-t/\tau_{th}} - e^{-\Gamma_A t}\cos(\omega_A t)\right) + B\left(e^{-t/\tau_{th}} - e^{-(t/\tau_s)^n}\right)$$
$$+ Ce^{-\Gamma_A t}\sin(\omega t) \quad (S15)$$

where A and B are ISTS amplitudes, C is the amplitude for the ISBS signal, τ_{th} is the thermal decay time, and τ_s is the characteristic structural relaxation time stretched by the exponent n. Finally, ω_A is the observed acoustic frequency, and Γ_A is the acoustic damping rate. In regimes of extremely low damping, the effect of finite pump and probe spot sizes was explicitly taken into account using the results of Yan and Nelson[S18] via a multiplication of the acoustic damping term by a factor $e^{-\sigma(\omega t/q)^2}$, where σ is given terms of the spot sizes of the probe beam σ_p and the excitation beam σ_e as

$$\sigma = \frac{\sigma_p + 2\sigma_e}{2\sigma_e\left(\sigma_p + \sigma_e\right)}. \quad (S16)$$

Figure S12 details a representative trace with $\Lambda = 24.9$ μm which shows excellent agreement with the model function, Eq. (S15). These data, plotted on a logarithmic time scale to cover signal extending over 6 decades, were taken in the regime where the alpha-relaxation dynamics extend to time scales significantly longer than that of the acoustic response, resulting in insignificant acoustic damping and slow components of thermal expansion that are observed directly in the data. This slow component is represented by the stretched exponential function in the time-domain signal function of Eq. (S15). In principle this slow signal reveals structural relaxation dynamics in the 0.1-100 μs temporal range and we could equate $\tau_s = \tau_\alpha$. However, in addition to structural relaxation dynamics, this component of the signal includes heat capacity relaxation dynamics that may yield a complicated
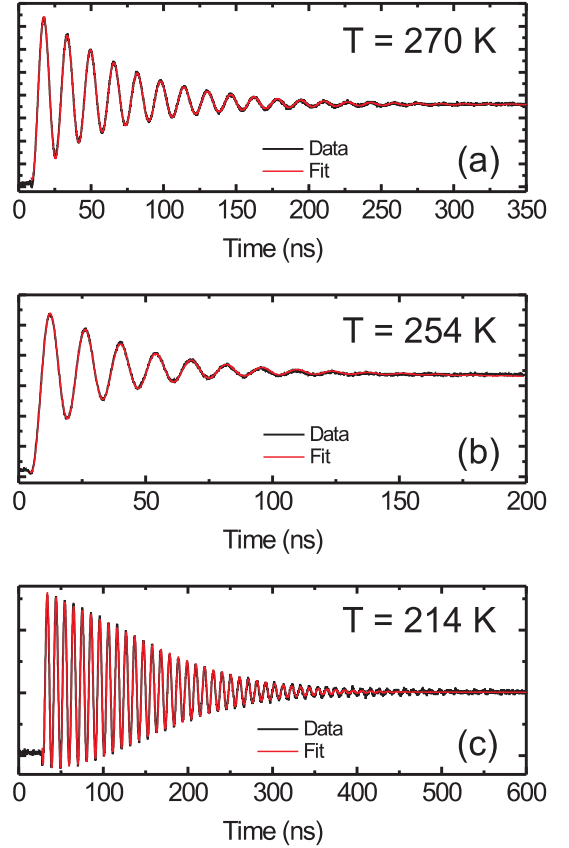

FIG. S13. ISTS signal in different temperature regimes using grating fringe spacing 24.9 μm. Fits are performed using Eq. S15. In (a), the sample is in the liquid state and damped acoustic oscillations are observed on the sub-μs timescale. (b) As the sample is cooled, both the frequency and damping rate increase due to the presence of the alpha-relaxation dynamics at the acoustic frequency. (c) Near T_g, the acoustic frequency is greatly increased and the damping rate decreased due to the solid characteristic of the material.

time-dependent evolution of the sample temperature at the heated interference maxima. We expect that this is a small contribution to the signal, but because we are not able to determine it through independent measurement, we did not use the slow component of our ISS data or the stretched exponential fits to them in construction of our modulus curves.

For this study we focused exclusively on the acoustic contribution. Figure S13 shows three more representative traces of ISTS data recorded with 24.9 μm grating spacing. In all traces there are oscillations due to counter-propagating acoustic waves. The data in (a) are taken in the high-temperature liquid state, showing weak damping of the acoustic wave. In the regime where the alpha-relaxation is on the time scale of an acoustic period, mechanical energy is quickly dissipated into structural relaxation and the acoustic signal is strongly damped, as shown in (b). Finally, when the liquid is cooled into the very viscous state as in (c), the damping rate is observed

to decrease significantly. Here the effects of finite beam spot sizes lead to non-exponential decay, which is modeled by the correction term described above.

The transient grating spacing (*i.e.*, wavevector magnitude q) can be varied by changing the phase mask pattern to make the excitation pulses cross at different angles in the sample, and new data can be recorded which will reveal different acoustic frequencies and damping rates as functions of temperature. Using these acoustic parameters determined at many wavevectors at a common temperature, the complex frequency-dependent longitudinal modulus $\hat{M}(\omega) = M'(\omega) + iM''(\omega)$ at that temperature can be determined from

$$M'(\omega) = \rho \frac{\omega^2 - \Gamma^2}{q^2} \tag{S17}$$

$$M''(\omega) = \rho \frac{2\omega\Gamma}{q^2}. \tag{S18}$$

The excitation beams were focused to a spot 2.5 mm in the grating dimension and 100 μm in the perpendicular dimension so that the acoustic waves would have many periods and the decay of signal would be due primarily to acoustic damping rather than propagation away from the excitation and probing region of the sample. In regions of extremely low damping the effects of finite spot size were taken into account, as detailed above. Damping rates as low as 2 μs^{-1} could be measured reliably.

The probe was focused to a spot of 1 mm in the grating dimension by 50 μm in the perpendicular dimension. We used a common phase mask optimized for diffraction into ± 1 orders at 800 nm for both pump and probe beams. The local oscillator was attenuated by a factor of 10^{-3}. Approximately 30% of the pump power was lost into zero order with this configuration, but the pump intensity still had to be reduced significantly to avoid unwanted nonlinear effects. The signal was collected with a fast amplified photodiode with 3 GHz bandwidth and processed in a 4 GHz bandwidth digitizing oscilloscope. When slower signals were studied, we used a New Focus Model 1801-FS detector with a bandwidth of DC to 125 MHz. Depending upon signal-to-noise ratios, signals from 2,000 to 4,000 repetitions of the measurement were averaged for each data trace, with total data acquisition times of less than a minute per trace.

The acoustic wavelength was calibrated through ISTS measurements in ethylene glycol, for which the speed of sound is known accurately[S19], and cross-checked with internal measurements of DC704 at high temperature where the speed of sound is constant across the range of measured acoustic wavelengths. This calibration was double-checked after all of the data collection was finished, and the variation in acoustic wavelength ranged from approximately 0.1% to 1.8%, with an average of 0.7%. This determined our uncertainties in the sound speeds, but did not affect the uncertainties in the damping rate.

To build acoustic spectra, data were taken by fixing the sample temperature and using every available phase mask pattern to provide wavelengths in the range from 1.75 μm to 101 μm. These grating spacings were 1.71 μm, 1.97 μm, 2.33 μm, 2.68 μm, 3.14 μm, 3.64 μm, 4.20 μm, 4.85 μm, 5.66 μm, 6.56 μm, 6.70 μm, 7.61 μm, 9.13 μm, 10.2 μm, 11.7 μm, 13.7 μm, 15.7 μm, 18.3 μm, 21.3 μm, 24.9 μm, 28.5 μm, 33.0 μm, 38.1 μm, 44.2 μm, 49.8 μm, 50.7 μm, 56.9 μm, 65.9 μm, 76.0 μm, 88.0 μm, and 101 μm. The procedure was repeated for different temperatures until the desired range was covered.

D. Time-Domain Brillouin Scattering ($\sim$3–23 GHz)

In time-domain Brillouin scattering (TDBS), acoustic wave propagation at low GHz frequencies is monitored by an optical, time delayed probe at a fixed wave vector and a complex frequency is measured. The detection scheme is based on the coupling of mechanical strain with laser light through the so-called photoelastic or Brillouin effect.
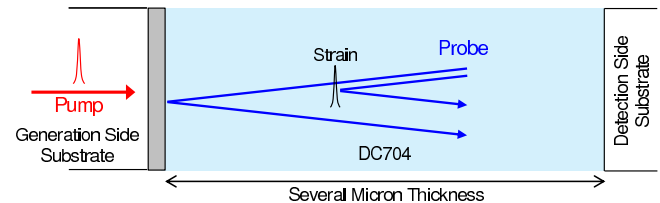

FIG. S14. Schematic diagram of time domain Brillouin scattering detection. An acoustic strain pulse is generated in a transducer film and propagates into an adjacent liquid layer. Incident probe light reflects off of the transducer film, but also off the propagating strain pulse due to acoustically induced local changes in the refractive index, and interference gives rise to an oscillatory modulation of the overall reflected probe intensity.

A schematic illustration of this technique is shown in Figure S14. Acoustic waves are excited by a sub-picosecond optical pump pulse which deposits energy in a photo-acoustic aluminum transducer thin film. The subsequent sudden thermal expansion launches an acoustic strain pulse $\eta(z, t)$ into the adjacent liquid film. Probing of the propagation and attenuation of the strain pulse away from the transducer is accomplished by a second optical pulse mechanically delayed by a variable time Δt relative to the pump. The reflected probe light consists of a number of superposing beams with a principal reflection from the transducer and minor reflections from the strain pulse[S9,S20]. These reflections arise from the local change in refractive index produced by the presence of the strain pulse via the photoelastic or Brillouin effect. Depending on the distance $d = c\Delta t$ of the strain pulse from the transducer film, the reflected beams interfere either constructively or destructively. This results in an oscillatory modulation of the total reflected intensity as a function of time, which can be used to determine the
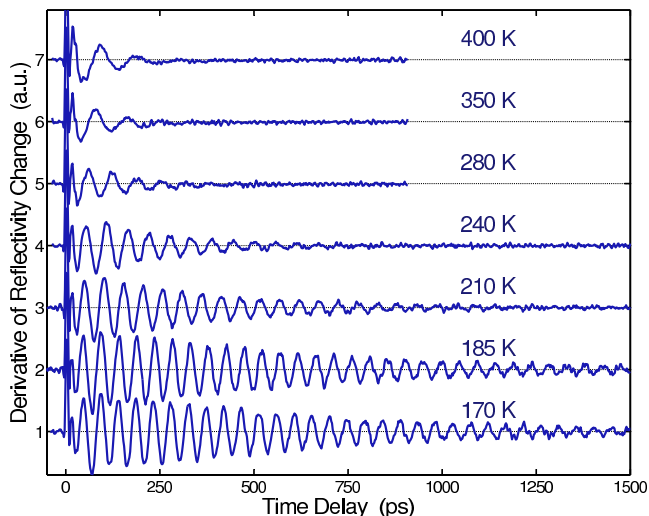
FIG. S15. Selection of Brillouin scattering data in DC704 recorded at various temperatures. At the highest temperatures, the frequency is lower and the damping rate higher due to the presence of complex relaxation dynamics at the probed frequency. As the temperature is reduced, the frequency is observed to increase and the damping rate is observed to decrease significantly.

acoustic speed c of the strain pulse in the sample while the amplitude of the modulation can be related to the amplitude of the strain.

At normal incidence of the probe beam with respect to the transducer, the measured Brillouin scattering frequency is

$$f_{BS} = \frac{2nc}{\lambda} \,, \tag{S19}$$

where n is the index of refraction and λ is the optical wavelength. A measurement of this frequency can thus give the sound velocity when the refractive index of the sample is known. To determine the acoustic attenuation rate at this frequency, the raw data were fit to the time-domain form of a damped oscillator, i.e., $e^{-\Gamma t}\sin(\omega t)$.

For the purpose of compiling broad relaxation spectra, we recorded time-domain Brillouin scattering data at many different temperatures with probe light at the laser fundamental wavelength, centered at 790 nm, and frequency doubled light, centered at 395 nm. The sample was constructed from a 20 nm aluminum transducer film on a sapphire generation-side substrate and a many-micron thick liquid layer held by another sapphire substrate. This construction allowed us to monitor the propagation of the acoustic strain pulse until it was attenuated to below our detection limit.

Selected raw data at several different temperatures are shown in Figure S15 and clearly illustrate the strong acoustic attenuation at temperatures above the glass transition temperature, $T_g = 210$ K. The attenuation rate is observed to decrease as the liquid is cooled into the glassy state. Results for the extracted Brillouin scat-

tering frequency and attenuation rate were obtained by fitting a Lorentzian oscillator as described above.

E. Picosecond Ultrasonic Interferometry (∼25-120 GHz)

Here we describe the manner in which a specialized picosecond laser ultrasonic technique may be combined with interferometric detection for probing longitudinal acoustic waves in the tens to hundreds of gigahertz frequency range. This method, depicted in Fig. S16, is performed in a similar sample geometry as in time-domain Brillouin scattering. Single-cycle acoustic waves are generated in a thin metal transducer film on one side of a liquid film and their arrival and shape is measured by a Sagnac interferometer[S21,S22] at the receiver metal film. In our analysis we compared transmitted strain pulses through different liquid thicknesses with each other in order to extract the liquid response at a fixed frequency.
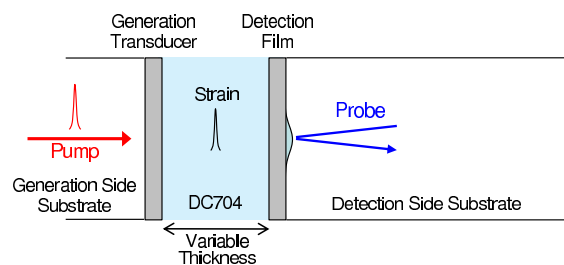

FIG. S16. Sketch of picosecond ultrasonic interferometric experimental approach. Energy deposition by an ultra-short laser pulse in a transducer film resulted in sudden thermal expansion and launched a compressional strain pulse into and through the DC704 liquid sample. Its arrival in a detection film caused a small displacement of that film which was detected interferometrically.

Our approach is to compare signals transmitted through different thicknesses of sample material. In a manner similar to the NAI experiment detailed in Sec. I B, we compare the amplitudes and phases at a given frequency by Fourier transformation of the two time-domain signals $h_1(t)$ and $h_2(t)$, which constitute two signals transmitted through different sample thicknesses d_1 and $d_2 > d_1$ (e.g., η_4 and η_{10} in Fig. S17).

Figure S17(a) shows a selection of the measured displacements for several different thicknesses of DC704. Typically, we measured the strain transmitted through about 50 different liquid thicknesses. A signal (η_0) from the part of the sample assembly where the transducer films were in contact is added to the plot. We did not use such signal amplitudes for our analysis since the acoustic strain in this case did not experience exactly the same conditions (due to the contact between the metal thin films) as in the other cases, but the signal provided calibration for essentially zero liquid thickness.

We assume that the displacement can be described by a plane wave equation. The time-derivative of the displace-
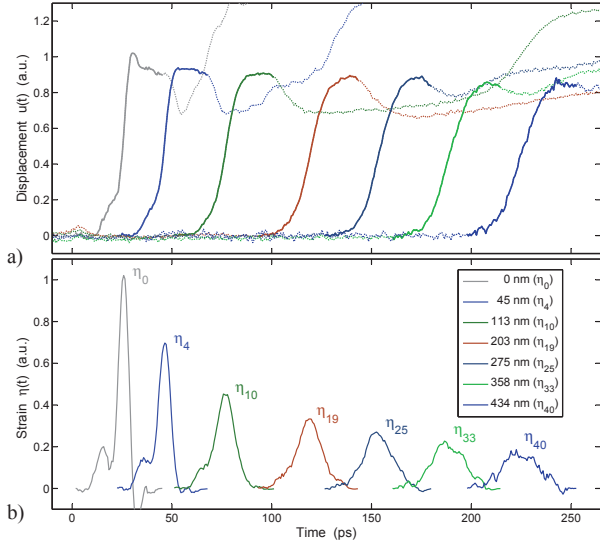
FIG. S17. Measured and normalized displacement data (a) and the derived strain (b) after transmission through different layer thicknesses of DC704 at 200 K. The acoustic strain was produced by a 30 nm aluminum transducer film on a sapphire generation side substrate and detected interferometrically at the back side of a 100 nm aluminum film on a sapphire detection side substrate. Signals labeled η_4, η_{10}, η_{19}, η_{25}, η_{33}, and η_{40} are from acoustic waves transmitted through progressively greater liquid thicknesses as indicated.

ment $u(t,x)$ is then proportional to the strain $\eta(t,x)$,

$$\eta(t,x) = \frac{d}{dx}u(t,x) = \frac{1}{c}\frac{d}{dt}u(t,x) . \qquad \text{(S20)}$$

where c is the acoustic phase velocity (assuming c is non-dispersive).

Figure S17(b) shows the transmitted strain through a selection of different liquid thicknesses, labeled η_4, η_{10}, η_{19}, η_{25}, η_{33}, and η_{40}. The shape of the strain after transmission through different liquid thicknesses is simply related to a set of acoustic parameters which includes the complex speed of sound or equivalently the complex longitudinal modulus. After traveling through an additional distance Δd in the liquid, the Fourier domain 'output' strain $\tilde{\eta}_{out}(\omega)$ is related to the 'input' strain $\tilde{\eta}_{in}(\omega)$ by the complex wavevector, $k(\omega) = \omega/c(\omega)$,

$$\tilde{\eta}_{out}(\omega) = e^{i\hat{k}(\omega)\Delta d}\,\tilde{\eta}_{in}(\omega) . \qquad \text{(S21)}$$

While the real portion of the wavevector shifts the phase of the input strain, the imaginary component of the wavevector dampens the amplitude. If we denote the transmitted strain as

$$\tilde{\eta}_{trans}(\omega) = \frac{\tilde{\eta}_{out}(\omega)}{\tilde{\eta}_{in}(\omega)} , \qquad \text{(S22)}$$

we can write the complex acoustic velocity as

$$c(\omega) = \frac{\omega}{k} = \frac{i\,\omega\,\Delta d}{\ln(\tilde{\eta}_{trans}(\omega))} . \qquad \text{(S23)}$$

From this, the complex acoustic modulus $M(\omega)$ and the acoustic compliance spectrum $J(\omega)$ can be determined directly from a broadband measurement of the transmitted strain:

$$M(\omega) = -\rho \left[\frac{\omega\,\Delta d}{\ln(\tilde{\eta}_{trans}(\omega))}\right]^2 . \qquad \text{(S24)}$$

In order to account for different attenuation strengths at different frequencies in the most reliable manner, we conducted our analysis on data sets having about 50 strain profiles, each recorded at a different liquid thickness using a fixed excitation pulse shape and at a constant sample temperature.

II. ANALYSIS OF MECHANICAL SPECTRA

Below we provide a more in-depth discussion of some of the fitting results presented in the main manuscript in the context of the mode coupling theory.

A. Time-temperature superposition

The relaxation behavior at frequencies around the alpha-peak was fitted by a stretched exponential equation

$$\chi(t) = \chi_0 + \Delta\chi \exp\left(-(t/\tau_\alpha)^n\right) , \qquad \text{(S25)}$$

where χ_0 denotes the long-time limit of $\chi(t)$ and $\Delta J\chi = \chi_0 - \chi_\infty$ the relaxation strength.

The $M''(\omega)$ data were fitted to a numerical Fourier transform of Eq. (S25) using a routine developed by Wuttke[S23], yielding the fits to the data in Fig. 2(a) of the main text. The compliance data $J'(\omega)$ and $J''(\omega)$ were also fit to the KWW Fourier transform using the same routine. In order to demonstrate TTS, rescaling of the compliance data was accomplished using our measured values for the limiting instantaneous speed of sound (c_∞)[S24] whose temperature dependence was found to be fit well by the form

$$c_\infty(T) = 3840[\text{m/s}] - 6.9[\text{m/sK}] \times T \qquad \text{(S26)}$$

to calculate $J_\infty = \sqrt{\rho/c_\infty}$ and the normalized quantities in Fig. 3(a).

The low-temperature compliance data cover the alpha relaxation spectrum quite thoroughly, and the alpha spectra were found to be fit well by the KWW form with the stretching exponent $n = 0.5$. This value was fixed for the fits at higher temperatures, leaving only the three remaining fitting parameters J_0, ΔJ, and τ_α. Restricting the number of fitting parameters made possible fitting of spectra across the modest frequency gaps in our spectra. We note that the measurements were typically conducted with small temperature steps (usually ~ 2 K) but the measurements conducted with different methods
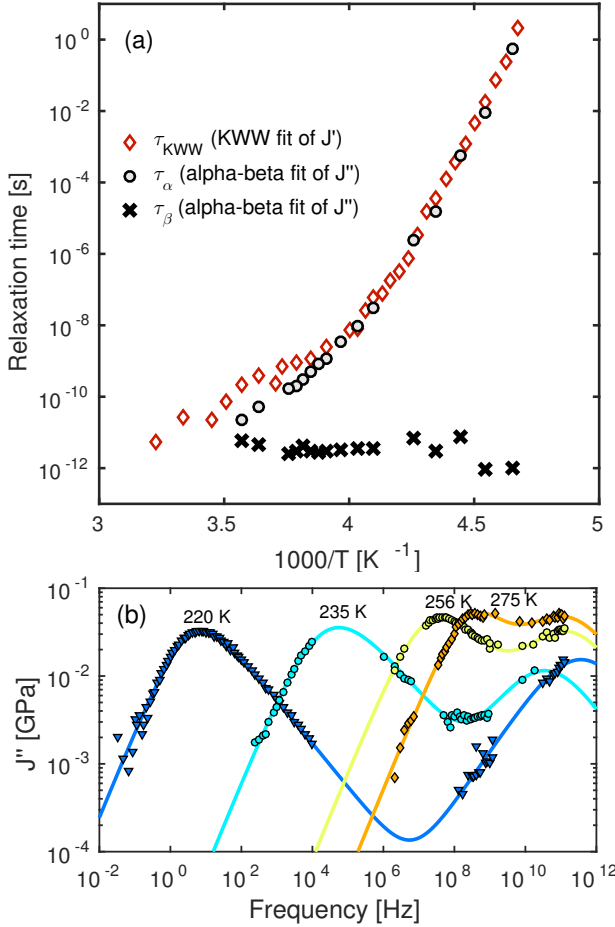
FIG. S18. (a) Relaxation times of the alpha and beta processes from fits of compliance data to a phenomenological alpha-beta merging model expressed as a network diagram[S25,S27]. The alpha relaxation times of the alpha-beta model are markedly non-Arrhenius and agree well with the $\tau_\alpha(t)$ values of the stretched exponential fit. The beta relaxation time is roughly temperature-independent. (b) Examples of fitted curves at selected temperatures.

were not all made at exactly the same temperatures. In order to show results spanning the entire frequency range at selected temperatures (e.g., 215 K, 225 K, and 235 K in Fig. 3a), we interpolated at the lower frequencies between data measured at very nearby temperatures, e.g., 214 K and 216 K for the results shown at 215 K. This procedure allowed us to reliably connect results from our highest to lowest frequency ranges despite the number of measurement methods involved.

The KWW form describes only alpha relaxation, not the faster beta relaxation dynamics which clearly appear in the imaginary compliance spectra $J''(\omega)$ at high frequencies. In order to extend our fits to this part of the spectra, we used an alpha-beta merging model that has been described elsewhere[S25,S26]. The fitted alpha and beta relaxation times from this model are shown in in Fig. S18(a) and we show examples of fitted curves in Fig. S18(b). The alpha relaxation times show excellent
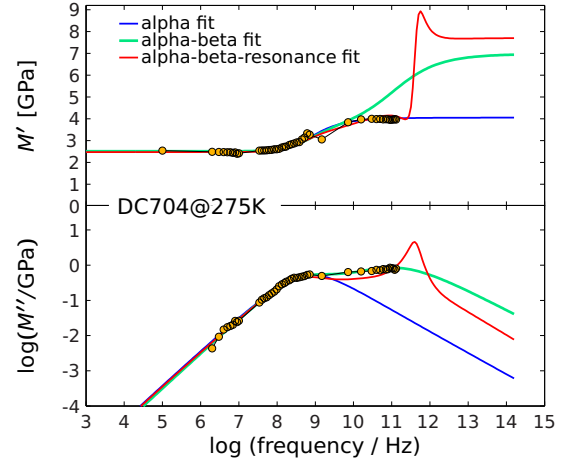

FIG. S19. The complex longitudinal modulus of DC704 at 275 K including several fitting schemes: the blue curve is a stretched exponential (Eq. (S25)) fit of the real part, the green curve is an alpha-beta model fit[S25,S26] to the imaginary part, and the red curve is a an alpha-beta model fit with an added resonance.

agreement with the τ_α values obtained from the stretched exponential fits. The beta relaxation time is nearly constant over the range of temperatures explored here, i.e., $\tau_\beta \sim 1$ ps, as expected. Although the alpha-beta model fits were not used to test MCT, they can provide insights based on their parameter values and on their implications for the connections between the real and imaginary parts of the compliance. Both the KWW and the alpha-beta fits are illustrated in Fig. S19 for a single temperature, 275 K. The alpha-beta model fit overshoots the real part dramatically at the highest frequencies. However, the resonance region is approached here, and we can add this to our alpha-beta model and obtain a curve that matches the rise in the imaginary part while the real part remains flat. This is shown in Fig. S19 in red. The fit is not perfect; the purpose here is merely to show that although beta relaxation is apparent in the imaginary spectrum only, the data do not violate the Kramers-Kronig relations. Owing to the consistency of the KWW fitting scheme with the alpha-beta analysis, as shown in Fig. S18, the KWW fits were used in Fig. 3(b) of the main text and the subsequent analysis.

B. Temperature dependent compliance minimum values

Using the fits described in the previous section, the imaginary compliance $J''(\omega)$ plots may be superposed upon each other by scaling the axes by the frequency minimum ω_{min} and the imaginary compliance value J''_{min}, shown in Fig. S20(a). The determined frequencies $\omega_{min}(T)$ and compliance values $J''_{min}(T)$ at the minima between the alpha and beta relaxation features may be used in conjunction with the dynamic exponent a to test additional MCT predictions. These predictions indicate
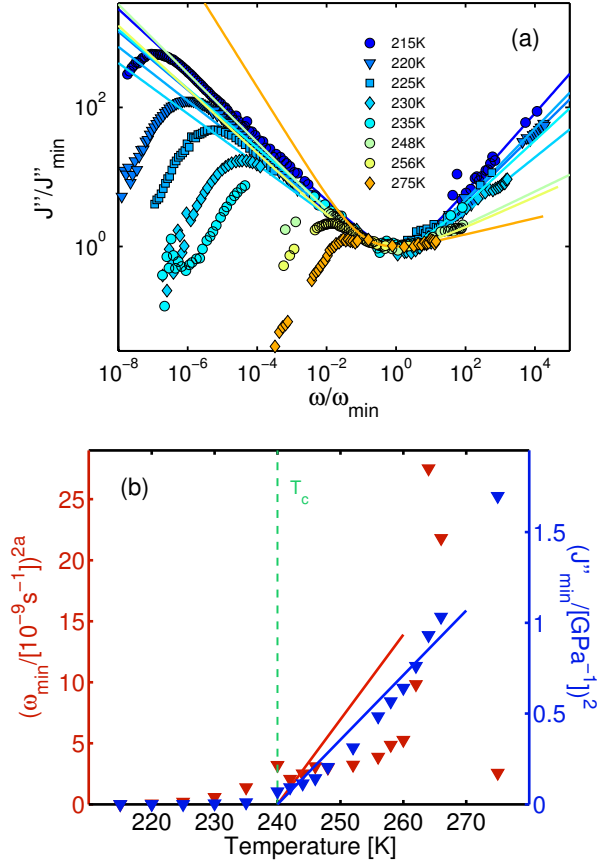
ters can be determined over a wide temperature range, but only the 240–248 K range is useful for comparison to MCT predictions. However, the uncertainties in $\omega_{\min}$ and $J''_{\min}$ make this assessment difficult.

[S1] T. Hecksher, N. B. Olsen, K. A. Nelson, J. C. Dyre, and T. Christensen, J. Chem. Phys. **138**, 12A543 (2013).

[S2] T. Christensen and N. B. Olsen, Phys. Rev. B **49**, 15396 (1994).

[S3] T. Christensen and N. B. Olsen, Rev. Sci. Instrum. **66**, 5019 (1995).

[S4] T. Hecksher, *Relaxation in supercooled liquids.*, Ph.D. thesis, Roskilde University (2010).

[S5] J. A. Johnson, *Optical Characterization of Complex Mechanical and Thermal Transport Properties*, Ph.D. thesis, Massachusetts Institute of Technology (2011).

[S6] Y.-X. Yan and K. A. Nelson, J. Chem. Phys. **87**, 6257 (1987).

[S7] S. M. Silence, A. R. Duggal, L. Dhar, and K. A. Nelson, J. Chem. Phys. **96**, 5448 (1992).

[S8] D. H. Torchinsky, *Optical Study of Shear and Longitudinal Acoustic Waves and Complex Relaxation Dynamics of Glass Forming Liquids*, PhD thesis, Massachusetts Institute of Technology, Cambridge, MA (2008).

[S9] C. Thomsen, H. Grahn, H. Maris, and J. Tauc, Phys. Rev. B **34**, 4129 (1986).

[S10] C. Klieber, *Ultrafast photo-acoustic spectroscopy of supercooled liquids*, Ph.D. thesis, Massachusetts Institute of Technology (2010).

[S11] J. D. Choi, T. Feurer, M. Yamaguchi, B. Paxton, and K. A. Nelson, Appl. Phys. Lett. **87**, 081907 (2005).

[S12] C. K. N. Patel and A. C. Tam, Rev. Mod. Phys **53**, 517 (1981).

[S13] A. Neubrand and P. Hess, J. Appl. Phys. **71**, 227 (1992).

[S14] P. Hess, App. Surf. Sci. **106**, 429 (1996).

[S15] C. Glorieux, J. D. Beers, E. H. Bentefour, K. V. de Rostyne, and K. A. Nelson, Rev. Sci. Instr. , 2906 (2004).

[S16] Y. Yang and K. A. Nelson, J. Chem. Phys. **103**, 7722 (1995).

[S17] G. Hinze, D. D. Brace, S. D. Gottke, and M. D. Fayer, J. Chem. Phys. **113**, 3723 (2000).

[S18] Y.-X. Yan and K. A. Nelson, J. Chem. Phys. **87**, 6240 (1987).

[S19] S. Silence, Ph.D. thesis, Massachusetts Institute of Technology (1991).

[S20] H. N. Lin, R. J. Stoner, H. J. Maris, and J. Tauc, J. Appl. Phys. **69**, 3816 (1991).

[S21] D. H. Hurley and O. B. Wright, Opt. Lett. **24**, 1305(3) (1999).

[S22] B. Perrin, C. Rossignol, B. Bonello, and J. Jeannet, Physica B: Cond. Matter **263-264**, 571 (1999).

[S23] J. Wuttke, Algorithms **5**, 604 (2012).

[S24] C. Klieber, T. Hecksher, T. Pezeril, D. H. Torchinsky, J. C. Dyre, and K. A. Nelson, J. Chem. Phys. **138**, 12A544 (2013).

[S25] N. Saglanmak, A. I. Nielsen, N. B. Olsen, J. C. Dyre, and K. Niss, J. Chem. Phys. **132**, 024503 (2010).

[S26] B. Jakobsen, K. Niss, C. Maggi, N. B. Olsen, T. Christensen, and J. C. Dyre, J. Non-Cryst. Solids **357**, 267 (2011).

[S27] B. Jakobsen, T. Hecksher, T. Christensen, N. B. Olsen, J. C. Dyre, and K. Niss, J. Chem. Phys. **136**, 081102 (2012).

FIG. S20. Test of mode-coupling theory predictions for the evolution of the susceptibility minimum $J''_{\min}(\omega_{\min})$. (a) $J''(\omega)$ rescaled at the susceptibility minimum. The fits are given to the asymptotic form given by Eq. (3) of the main text. (b) $(\omega_{\min})^{2a}$ and $(J''_{\min})^2$ vs T. $T_c = 240$ K is marked by the vertical dashed line, and linear fits (keeping T_c fixed) to temperatures in the range from 240 K to 248 K are shown as solid lines.

the scaling of the imaginary susceptibility minimum as $\chi''(\omega_{\min}) \propto |T - T_c|^{1/2}$ and of the minimum frequency as $\omega_{\min} \propto |T - T_c|^{1/2a}$. In Fig. S20(b) we plot both $(J''_{\min})^2$ and $(\omega_{\min}(T))^{2a}$ versus temperature. The lines shown are the predictions of MCT based on the value $T_c = 240$ K. As in Figs. 5(b)–5(d) of the main paper, the parame-